Journal of Industrial Technology and Innovation 1(1) (2022) 246558

Computational Soliton Modulated Nonlinear Microring Add-drop Multiplexer and Potential Applications

M. Bunruangses[1], Mahdi Bahadoran[2], Nhat Truong Pham[3,4], P. Youplao[5], K. Ray[6] and P. Yupapin[7,*]

[1]Department of Computer Engineering, Faculty of Industrial Education, Rajamangala University of Technology Phra Nakhon, Bangkok 10300, Thailand

[2]Department of Physics, Shiraz University of Technology, 31371555, Shiraz, Fars, Iran

[3]Division of Computational Mechatronics, Institute for Computational Science, Ton Duc Thang University, Ho Chi Minh City, Vietnam

[4]Faculty of Electrical and Electronics Engineering, Ton Duc Thang University, Ho Chi Minh City, Vietnam

[5]Department of Electrical Engineering, Faculty of Industry and Technology, Rajamangala University of Technology Isan Sakon Nakhon Campus, Sakon Nakhon 47160, Thailand

[6]Amity School of Applied Sciences, Amity University Rajasthan, Jaipur, India

[7]Department of Electrical Technology, Sakonnakhon Technical College, School of Industrial Technology, Institute of Vocational Education Northeastern Region 2, Sakonnakhon, Thailand

***Corresponding author E-mail:** preecha@techsakon.ac.th

https://doi.org/10.55674/snrujiti.v1i1.246558

Received: 30 April 2022	Revised: 10 June 2022	Accepted: 27 June 2022	Available online: 1 July 2022

Abstract

This paper proposed the design of the multiplexer node for the free-space transmission link. Various soliton modulated signal categories are numerically studied. The proposed system is a modified micro-optical add-drop multiplexer. The cross phase modulated signals induced into the main ring by the two side rings can give more signal complexity, which can lead to having the securely transmitted signal requirement. The high optical power obtained from the soliton aspect can give long-distance communication, where the required frequency band can be improved and suitable for the required applications. For an instant, the use for the side road connection of the vehicle-to-everything (V2X) can be implemented in either cable or wireless(free-space) connection. The results obtained have shown promising applications such as free-space transmission link in both above and underground nodes, quantum cryptography, and communication security based on nonlinear aspects. Moreover, the electro-optic conversion

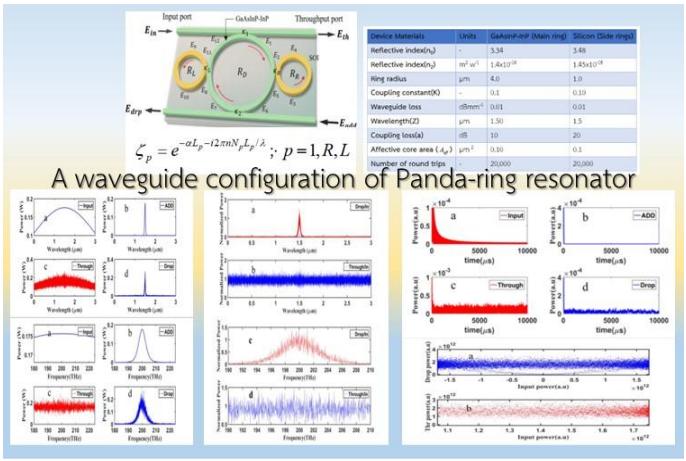

can also be used by the stacked layers of silicon-graphene-gold, in which the signal conversion can be applied suitably.

Keywords: Nonlinear device, Soliton communication, Soliton modulation, Add-drop multiplexer, Free-space communication

1. Introduction

Light-Fidelity (LiFi) is an important wireless technology in infrared and visible light spectrum communications for high data rate transmission [1-5]. Nowadays, it is considered to be a part of the visible light communication IEEE 802.15.7 standard [6, 7], which is attracting both industrial and academic researchers. LiFi is a networking paradigm that presents high-performance enhancements because it is an attractive backup option to be used for networking setup on the internet of things and its indoor capabilities [8-10]. Li-Fi enables the transmission of data through illumination by using a light-emitting diode with a light bulb that varies in intensity. Advantages of LiFi are high transmission data rate up to 10 Gb/s, intolerant to disturbances, more secure, integrated into medical devices, high transmit/receive power, high broad-spectrum bandwidth, a high device to device connectivity, and it can be used in all locations in compared with radio waves [11-13]. LiFi systems use the following modulation techniques that are named on-off keying, variable pulse position modulation, color shift keying, subcarrier inverse pulse position modulation, frequency shift keying, and subcarrier index modulation orthogonal frequency division multiplexing [14-18]. Vehicle to everything (V2X) communications refer to schemes for passing information flows in different applications of intelligent transportation information systems, which related to information traffic safety, operation efficiency and basic automated driving [19-22]. As well as V2X includes vehicle to vehicle (V2V), a vehicle to the network (V2N), a vehicle to Pedestrian (V2P), and vehicle to road infrastructure (V2I) communications. There are V2X communication technologies such as IEEE 802.11p, which is an adaptation of the IEEE 802.11 standard to address dynamic vehicular environments, and 3GPP C-V2X, which has been introduced in Release 14 of the long-term evolution standard [23-27]. There are many applications in vehicular networks which are divided into road safety and traffic efficiency with different performance requirements [28-30]. Vehicle-to-vehicle communications outline road safety applications requires low time delay quality of service and high system reliability [31-33]. In this article, the use of soliton modulation within a tiny device known as a nonlinear add-drop

multiplexer, which is a microring integrated circuit. The circuit is designed with practical parameters, where the computational results have been demonstrated and discussed for free-space transmission. The input carrier is modulated by the external source, which is a soliton via the add port, from which the multiplexed output can be applied to link with the long-distance transmission in either cable or free space. The required output can be filtered and obtained by the drop port output. It is suitable to link between the communication nodes of the side road of the vehicular-to-everything, where the channel capacity of the 5G is required. The information security concept is also available, which can be added and retrieved via the device ports. The node itself is the plasmonic antenna, in which the electro-optic conversion is available for both applications. The results obtained have shown interesting features that can be reliably used for V2X applications.

2. Theoretical Background

The nonlinear microring is configured to form the free-space side road transmission, which is a capability fabrication structure. Of course, the high power and broadband are required for such an application. We have proposed to use the optical circuit as shown in Figure 1, while the applied light source and modulator are given by the following details. The nonlinear microring is configured to form the free-space side road transmission, which is a capability fabrication structure. Of course, the high power and broadband are required for such application. We have proposed to use the optical circuit as shown in Figure 1, while the applied light source and modulator are given by the following details. The configuration of a modified nonlinear microring add-drop multiplexer known as nonlinear Panda-ring resonator is demonstrated in Figure 1. The nonlinear response of light through Panda-ring resonator is studied under various input pulses including continuous wave, dark and bright soliton. The general form of the Gaussian pulse, bright soliton, dark soliton and plane wave are given by the following equations.

$$P_{Gaussian} = \sqrt{2a^2}^{\left(-\frac{\lambda^2}{2\lambda_0^2}\right)}, \tag{1}$$

$$P_{Bright} = \sqrt{2a^2}\,\mathrm{Sech}^2\left(\sqrt{2a^2}\lambda\right), \tag{2}$$

$$P_{Dark} = \sqrt{2a^2}\,\mathrm{Tanh}^2\left(\sqrt{2a^2}\lambda\right), \tag{3}$$

$$P_{PW} = \sqrt{2a^2}^{\left(\frac{2\pi i}{\lambda}[x-ct]\right)}, \tag{4}$$

where a represents the optical field amplitude, λ shows the wavelength and λ_0 is the center wavelength of the input light. The direction of light propagation is displayed by x, the

speed of light and time are shown by c and t, respectively. The resonant condition can be obtained when the effective refractive index being equal to an integer number of the input light wavelength $n_{eff}L = m\lambda$. Two beams of light simultaneously fed into the Panda-ring resonator via up and down coupling regions (k_1 and k_2) are as shown in Figure 1. Based on the coupling strength of each coupling region, k_n, a fraction of the input light $iS_n = i\sqrt{(1-\gamma_n)k_n}$ will couple into the main ring of the Panda-ring and the remaining portion $C_n = \sqrt{(1-\gamma_n)(1-k_n)}$ goes straight to the output port. Here, $\gamma_n\left(n=1,2,R,L\right)$ corresponds to the intensity loss, and $k_n\left(n=1,2,R,L\right)$ denotes the coupling strength in each coupling region. According to the scattering matrix method [34], the following relationship can depict the electric fields inside the Panda-ring resonator.

$$\begin{cases} E_{th} = C_1E_{in} + iS_1E_{11}\sqrt[4]{\zeta_1} \\ E_1 = iS_1E_{in} + C_1E_{11}\sqrt[4]{\zeta_1} \\ E_7 = C_2E_5\sqrt[4]{\zeta_1} + iS_2E_{add} \\ E_{drp} = iS_2E_5\sqrt[4]{\zeta_1} + C_2E_{add} \\ E_5 = C_RE_1\sqrt[4]{\zeta_1} + iS_RE_3\zeta_R \\ E_3 = iS_RE_1\sqrt[4]{\zeta_1} + C_RE_3\zeta_R \\ E_{11} = C_LE_7\sqrt[4]{\zeta_1} + iS_LE_9\zeta_L \\ E_9 = iS_LE_7\sqrt[4]{\zeta_1} + C_LE_9\zeta_L \end{cases} \tag{5}$$

Here, ζ corresponds to the optical attenuation rates in each ring which is given by [35, 36, 37]

$$\zeta_p = e^{-\alpha L_p - i2\pi n N_p L_p/\lambda};\ p=1,R,L \tag{6}$$

where 1, R and L refer to the main ring, lateral small rings at right and left side of the Panda-ring resonator, respectively. Here α is the waveguide loss for whispering gallery modes, L_1, L_L, L_R are the circumferences of the main, left and right microrings in the system. The mode orders of the main, left and right microrings are demonstrated by N_1, N_L, N_R, respectively. The waveguide refractive index is given by $n = n_0 + n_2 I / A_{eff}$ where n_0, n_2, I and A_{eff} are the linear refractive index, the nonlinear refractive index, the optical intensity and the effective mode core area of the rings, respectively.

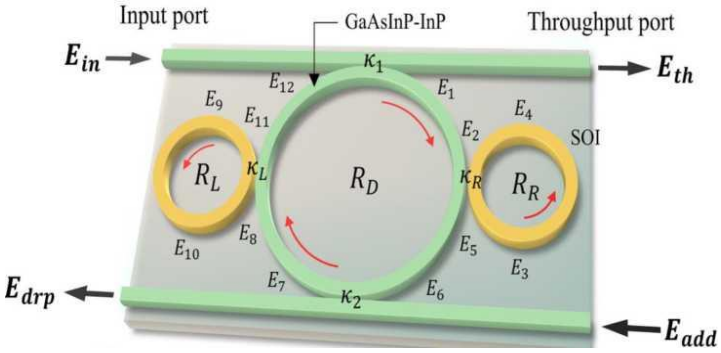

Figure 1: A waveguide configuration of Panda-ring resonator, where $E_{in}, E_{th}, E_{drp}, E_{add}$ are the electrical fields of the input, throughput, drop and add ports, R_L and R_R are the ring radii of the left and right rings, respectively. k_1, k_2, k_L, k_R: the coupling coefficients are. E_i: the electrical fields. The main ring is the GaAsInP-InP, the side ring is a silicon-on-insulator (SOI).

3. Simulation Results

A modulated soliton source using a Panda-ring circuit is formed by the GaAsInP-InP material waveguide, where the main and side rings are by SOI materials. The GaAsInP-InP ring of the Panda-ring (main ring) has a linear refractive index of n_0 is 3.34, a nonlinear refractive index is 1.4x10^{-16} m^{2}w^{-1} [36] with radius of R_m = 4 μm, the effective mode core area of A_{eff} = 0.1μm^2, the coupling strength of $k_1 = k_2 = 0.1$, the coupler loss and the waveguide field loss coefficient of $\gamma = 0.01$ and $\alpha = 10$ dBcm^{-1}, respectively. The small lateral rings have the radii of $R_R = R_L = 1$ μm, where the linear and nonlinear refractive indices of 3.48 and is 14.5 x10^{-18} m^{2}w^{-1} [38], respectively. The coupling strengths, coupler losses, and the effective mode core area of the small rings are the same as the main ring. However, the silicon-on-insulator waveguide applied in small lateral rings has the field loss coefficient of $\alpha = 20$ dBcm^{-1}. The simulation results are obtained using the MATLAB program. The resonant results are obtained with the 20,000 roundtrips.

3.1 The first category

A bright soliton with center wavelength of $\lambda_0 = 1.5$ μm entered into the input port and at the same time, a Gaussian pulse with $\lambda_0 = 1.5$ μm fed into the add port of the proposed Panda-ring system. The used parameters are as shown in Table 1. The effect of nonlinear refractive index can be detected after 20,000 round trip propagation of both signals via Panda rings and the nonlinear Kerr effect leads to the detection of chaotic output signals.

The change of refractive index brings about the change in the phase shift of the propagating pulse, which causes a nonlinear Kerr effect. This nonlinearity inside the ring resonator causes the generation of chaotic output signals as shown in Figures 2(b) and 2(c). The Gaussian and bright soliton are applied in the frequency domains, where the Panda-ring's output frequency responses are simulated as shown in Figure 3. The normalized output to input powers versus wavelength and frequency are shown in Figure 4. The signals are chaotic and the maximum peak round wavelength of 1.5 pm corresponds to the frequency range of 200 THz. The signals in time domains can be achieved by taking fast Fourier transform (FFT) from the results of frequency domain as simulated in Figures 5-7. The input Gaussian beam, Bright soliton at add port, the chaotic signals at through and drop ports are simulated in the time domain in Figure 5. Results in Figures 5, 6 and 7 are simulated for a time span of 0-10,000 μs, 0-300 μs, 3000-3100 μm, respectively. The nonlinearity response of an optical device can be monitored by considering the response of the system at the output port against the input port response. For this sake, the response of the Panda-ring resonator is simulated as shown in Figure 8. The system will be chaotic in all ranges and by increasing the input power, the chaotic peaks in the output power also get intensified.

Table 1: The used bright and dark soliton system parameters.

Device Materials	Units	GaAsInP-InP (Main ring)	Silicon (Side rings)
Reflective index(n_0)	-	3.34	3.48
Reflective index(n_2)	$m^2\ w^{-1}$	$1.4x10^{-16}$	$1.45x10^{-18}$
Ring radius	μm	4.0	1.0
Coupling constant(K)	-	0.1	0.10
Waveguide loss	$dBmm^{-1}$	0.01	0.01
Wavelength(Z)	μm	1.50	1.5
Coupling loss(a)	dB	10	20
Affective core area (A_{eff})	μm^2	0.10	0.1
Number of round trips	-	20,000	20,000

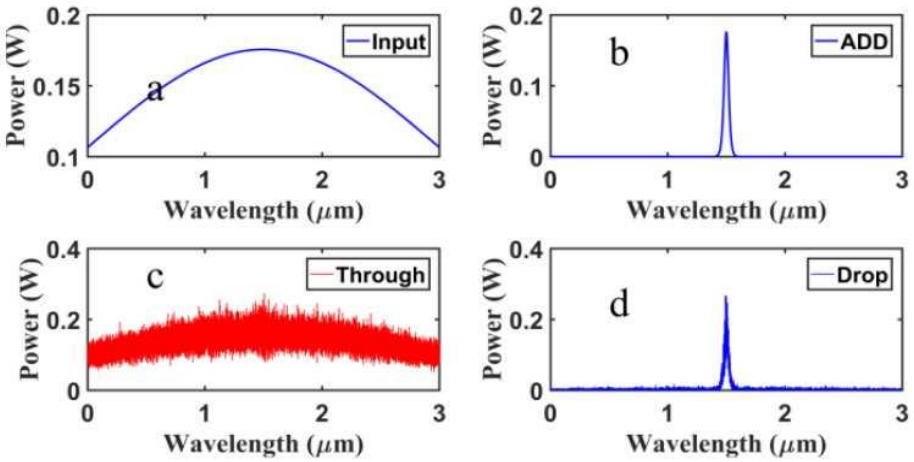

Figure 2: The signal responses versus wavelength, where(a) a Gaussian beam fed into the input port, (b) bright soliton in add port, (c) chaotic signal at through port, and(d) chaotic bright soliton at drop port.

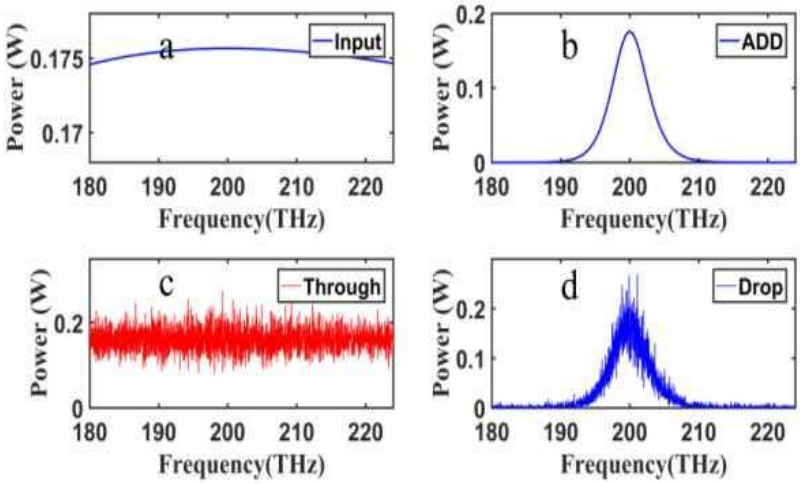

Figure 3: The frequency responses of Panda-ring resonator, where (a) a Gaussian beam fed into the input port, (b) bright soliton in add port, (c) chaotic signal at through port and (d) chaotic bright soliton at drop port.

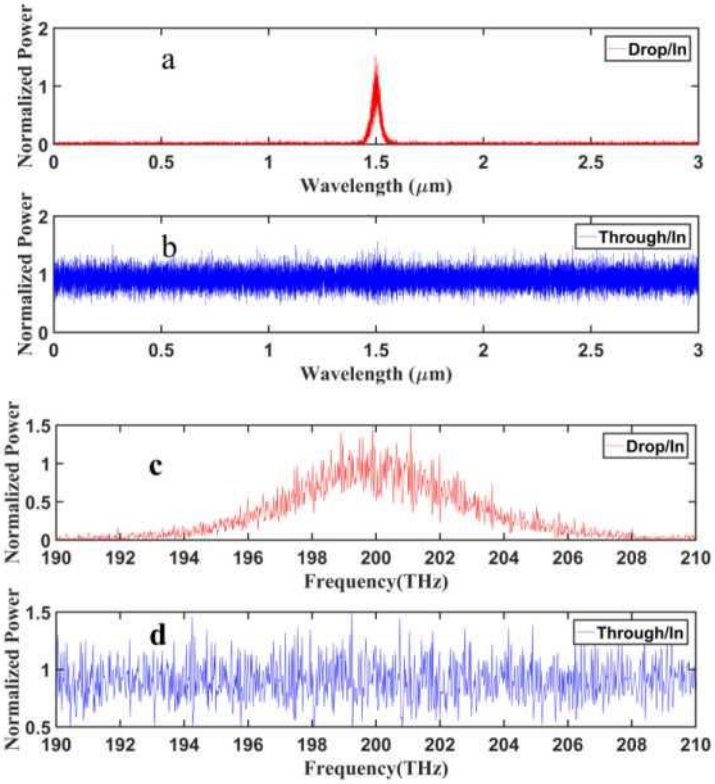

Figure 4: The normalized power versus wavelength, where (a) drop power to input power ratio, (b) chaotic signals of the through port to input power ratio. The frequency responses of Panda-ring resonator, where (c) drop power to input power ratio, and (d) chaotic signals of the through port to input power ratio.

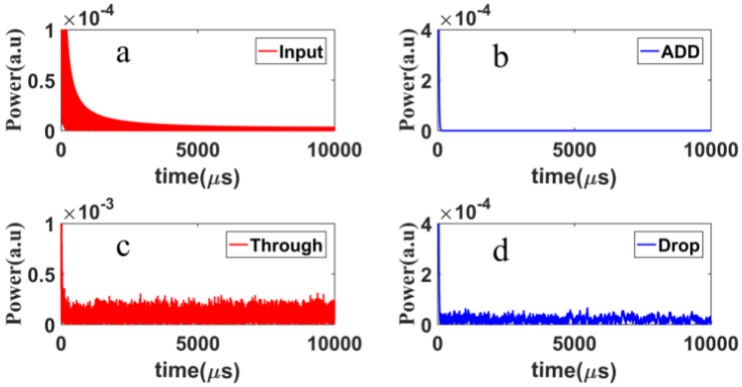

Figure 5: The signals in the time domain (time span 0-10,000 μs) of a Panda-ring resonator for (a) Gaussian beam fed into the input port, (b) bright soliton in add port, (c) chaotic signal at through port and (d) chaotic bright soliton at drop port.

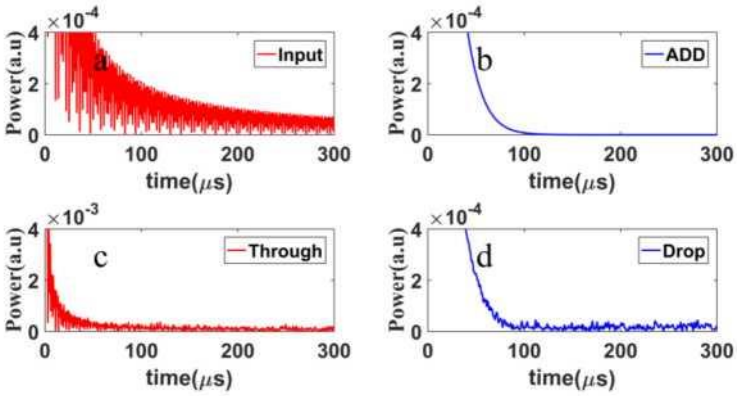

Figure 6: The signals in time domain (time span 0-300 μs) of a Panda-ring resonator for (a) Gaussian beam fed into the input port, (b) bright soliton in add port, (c) chaotic signal at through port and(d) chaotic bright soliton at drop port.

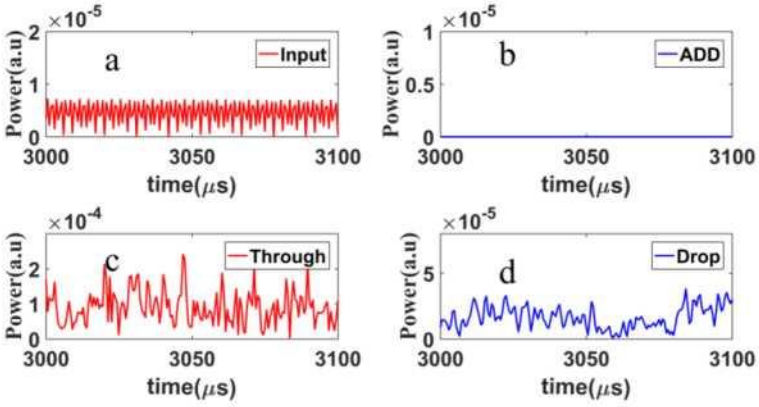

Figure 7: The signals in the time domain (time span 3,000-3,100 μs) of a Panda-ring resonator for (a) Gaussian beam fed into the input port, (b) bright soliton in add port, (c) chaotic signal at through port and (d) chaotic bright soliton at drop port.

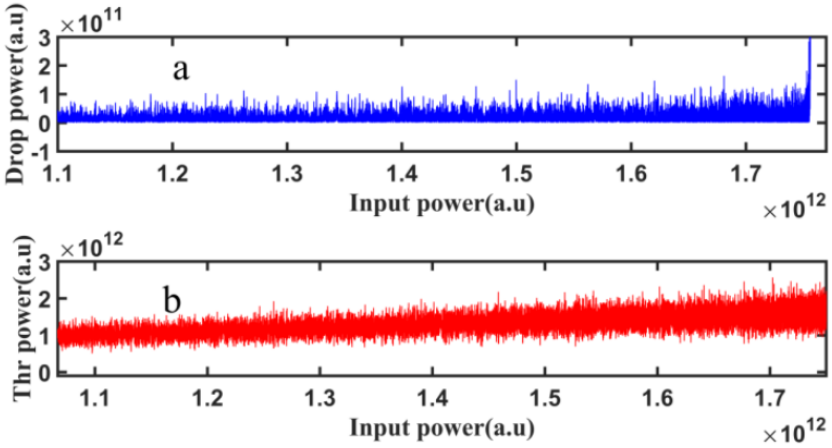

Figure 8: Bifurcation response of the Panda-ring resonator.

3.2 The second category

A plane wave, Eq. (4), with the wavelength of $\lambda_0 = 1.5$ μm fed into the input port of Panda-ring resonator and simultaneously a bright soliton, Eq. (2), with the center wavelength of $\lambda_0 = 1.5$ μm is coupled into the add port. The input light and the add port pulses in wavelength and frequency domains are simulated in Figures 9 and 10. The output to plane wave power against wavelength and frequency are shown in Figure 11. A specific optical tweezer(pulse) can be generated at 1.5 μm. The system undergoes a transition from bifurcation to biostability, then realized the stability interval 1,501-1,509 nm. The signals are chaotic but they are some on and off stability points of the system with a period of 10 THz. It means that the combination of plane wave and bright soliton through a Panda-ring resonator provides a trade-off between stability and bifurcation in the system that potentially can be used for secured optical communication. A plane wave at the input port and a bright soliton at add port have been entered into the Panda-ring resonator and the chaotic signals at through and drop ports are simulated in a time domain in Figures 12, 13 and 14. The results are shown for the different time span of 0-5,000 μs, 0-300 μs, 3000-3100 μm, respectively. A powerful signal and some chirped signals in the time domain can be realized from the output of Panda-ring resonator. The nonlinearity response of the Panda-ring in the second category is simulated in Figure 14. The last category focused on the Panda-ring response for an input plane wave, Eq. (4), with the wavelength of 1.5 pm and a dark soliton, Eq. (3), with center wavelength of 1.5 μm is input at the add port, where the modulation is formed. The input light and the add port pulses in wavelength and frequency domains are simulated in Figures 15 and 16.

The output to plane wave power against wavelength and frequency for the third category are shown in Figure 17, where the output is the chaotic signals. but periodic stability states are recognized for this case. Here the system experienced a conversion from bifurcation to biostability then realized the stability interval 1,497-1,503 nm and 1,500-1,506 nm at drop port and through port, respectively. On the other hand, an arrangement of plane wave and dark soliton in a Panda-ring resonator provides periodic stability and bifurcation in the system that is tunable and practical in optical communication security. A plane wave at an input port and a dark soliton at add port have been entered into the Panda-ring resonator and the chaotic signals at through and drop ports are simulated in a time domain as shown in Figures 18, 19 and 20. The results are shown for the different time span of 0-5,000 μs, 0-300 μs, 3,000-3,100 μs, respectively. A powerful signal and some chirped signals in the time

domain can be realized from an output of Panda-ring resonator. The nonlinearity response of the Panda-ring resonator in the second category is simulated as shown in Figure 21. As shown in Figure 21, for low power input and low power drop port signals there exists a stable and short-lived area.

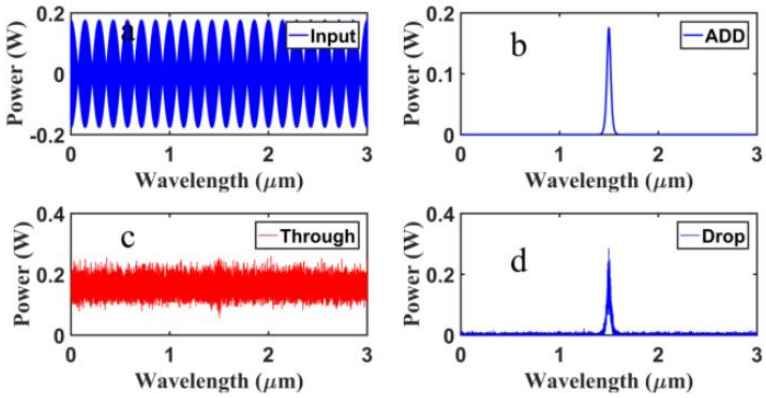

Figure 9: The signal responses versus wavelength, where (a) plane wave at the input port, (b) bright soliton at the add port, (c) chaotic signal at through port, (d) chaotic bright soliton at drop port.

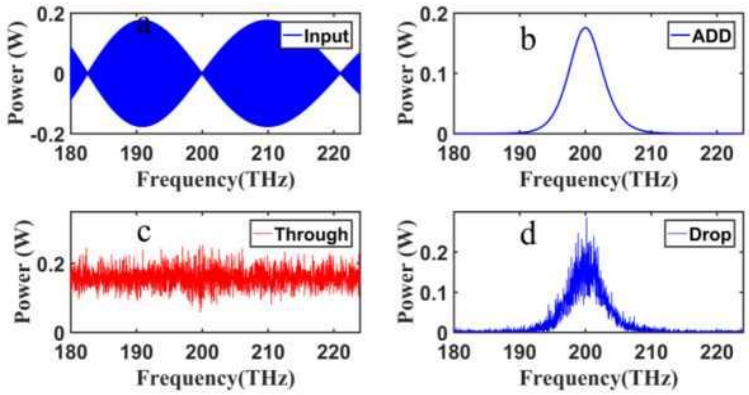

Figure 10: The frequency response of a Panda-ring resonator, where (a) plane wave at the input port, (b) bright soliton at the add port, (c) chaotic signal at through port, (d) chaotic bright soliton at drop port.

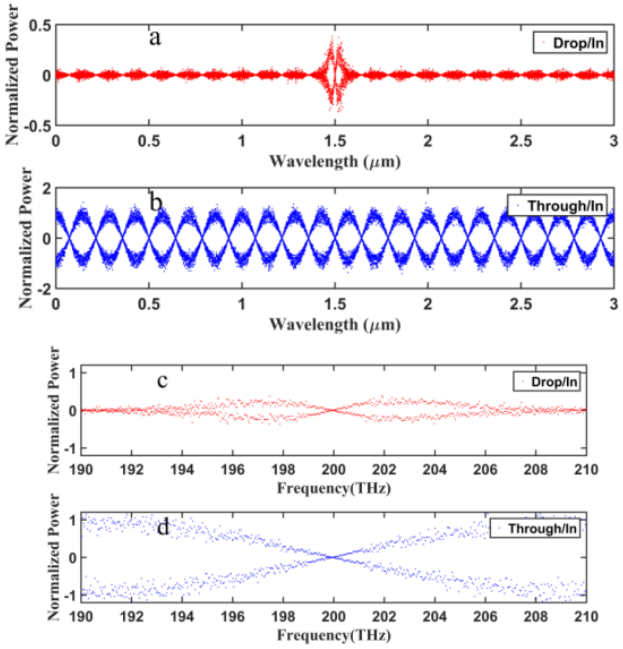

Figure 11: The output to plane wave power versus wavelength, where (a) drop power to input plane wave ratio, (b) chaotic signals of the through port to the input plane wave power ratio. The frequency responses of Panda-ring resonator for (c) drop power to input plane wave power ratio and (d) chaotic signals of the through port to the input power ratio.

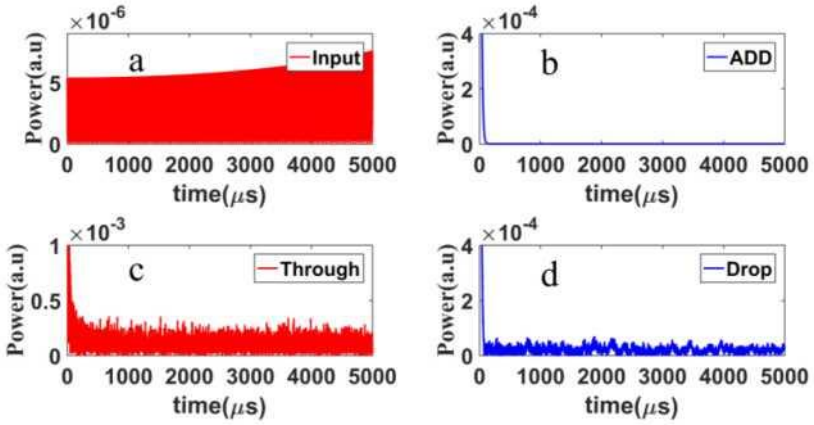

Figure 12: The signals in time domain (time span 0-5,000 μs) of a Panda-ring resonator for (a) plane wave coupled into the input port, (b) bright soliton in add port, (c) chaotic signal at through port and (d) chaotic bright soliton at drop port.

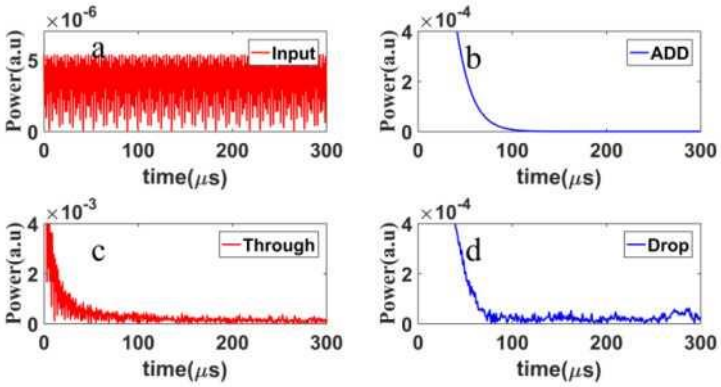

Figure 13: The signals in time domain (time span 0-300 μs) of a Panda-ring resonator for (a) plane wave coupled into the input port, (b) bright soliton in add port, (c) chaotic signal at through port and (d) chaotic bright soliton at drop port.

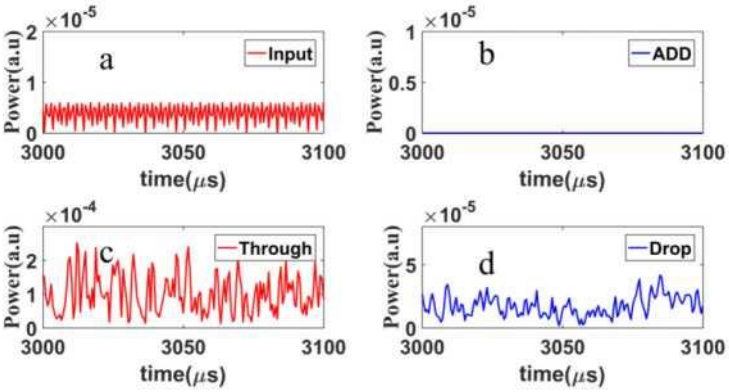

Figure 14: The signals in time domain (time span 3,000-3,100 μs) of a Panda-ring resonator for (a) plane wave coupled into the input port, (b) bright soliton in add port, (c) chaotic signal at through port and(d) chaotic bright soliton at drop port.

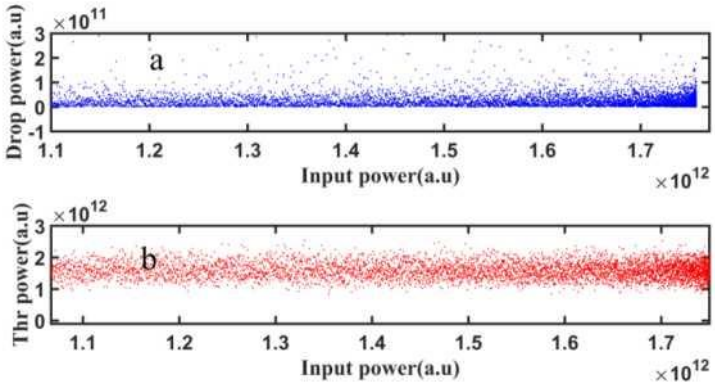

Figure 15: Panda-ring's response for plane wave input light and bright soliton at add port, where (a) drop against input and (b) through against input.

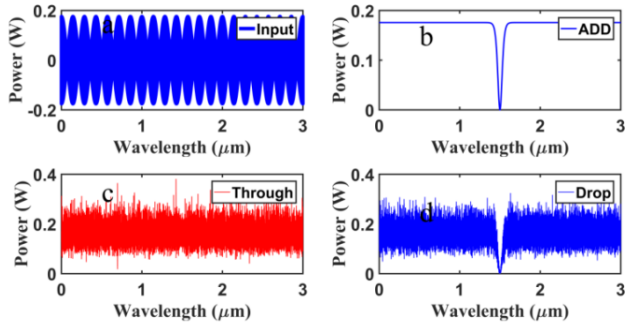

Figure 16: The signal responses versus wavelength, where (a) plane wave at the input port, (b) dark soliton at the add port, (c) chaotic signal at through port and(d) chaotic dark soliton at drop port.

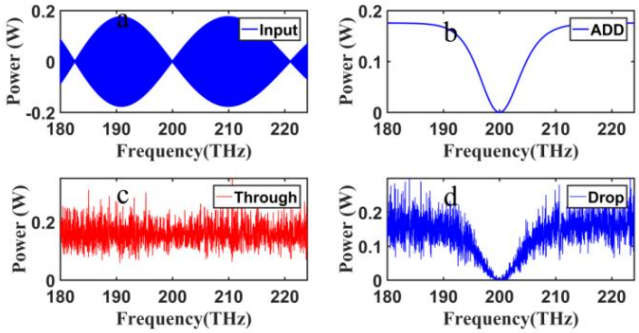

Figure 17: The frequency response of a Panda-ring resonator, where (a) plane wave at the input port, (b) dark soliton at the add port, (c) chaotic signal at through port and(d) chaotic dark soliton at drop port.

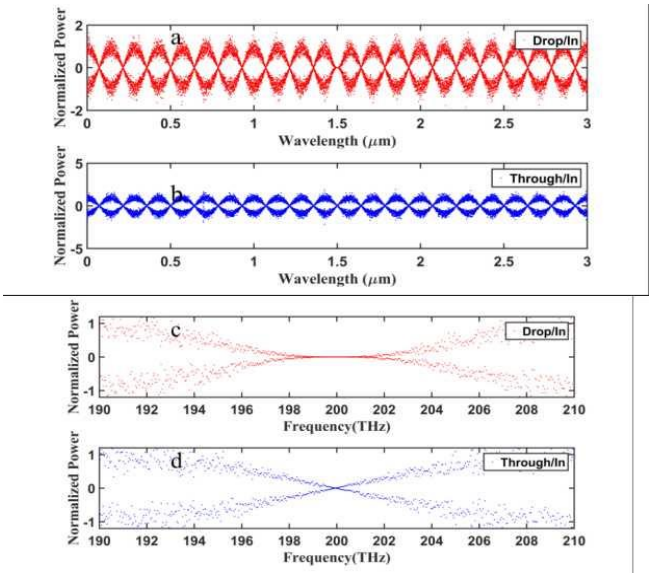

Figure 18: The Panda-ring normalized power in the 2nd category versus wavelength, where (a) drop power to input plane wave ratio, (b) chaotic through power to input plane wave power ratio. The frequency responses of Panda-ring resonator for (c) drop power to input plane wave power ratio and(d) chaotic through to input power ratio.

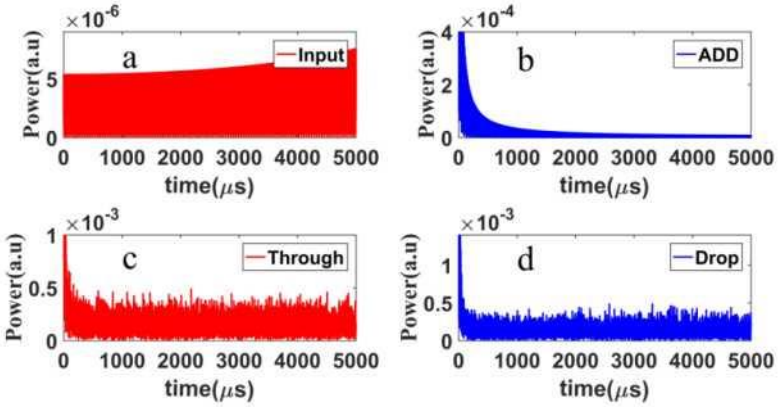

Figure 19: The signals in time domain (time span 0-5,000 μs) of a Panda-ring resonator for (a) plane wave coupled into the input port, (b) bright soliton in add port, (c) chaotic signal at through port and (d) chaotic bright soliton at drop port.

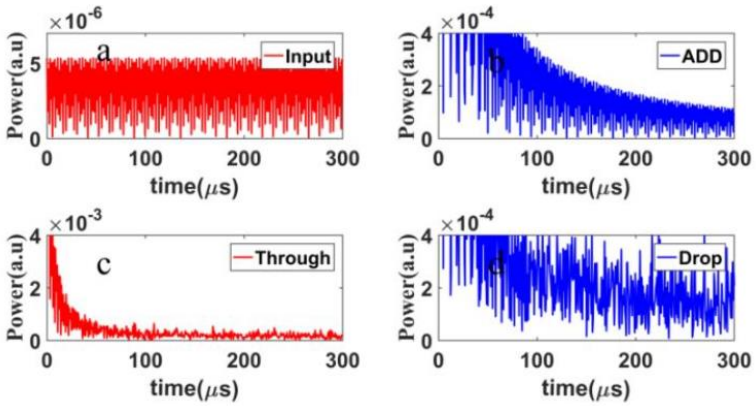

Figure 20: The signals in time domain (time span 0-300 μs) of a Panda-ring resonator for (a) plane wave coupled into the input port, (b) bright soliton in add port, (c) chaotic signal at through port and(d) chaotic bright soliton at drop port.

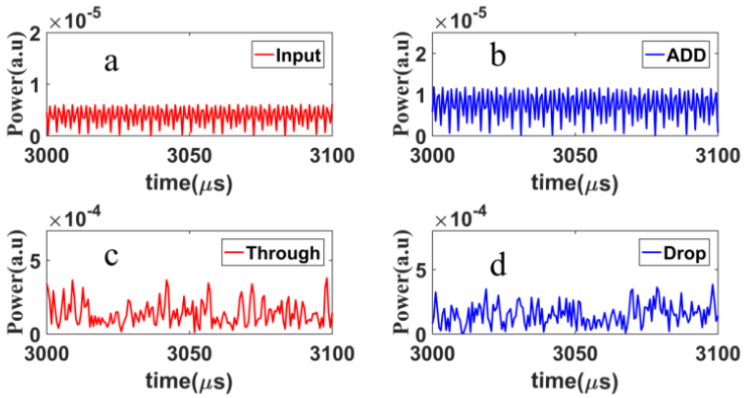

Figure 21: The signals in time domain (time span 3,000-3,100 μs) of a Panda-ring resonator for (a) plane wave coupled into the input port, (b) bright soliton in add port, (c) chaotic signal at through port and (d) chaotic bright soliton at drop port.

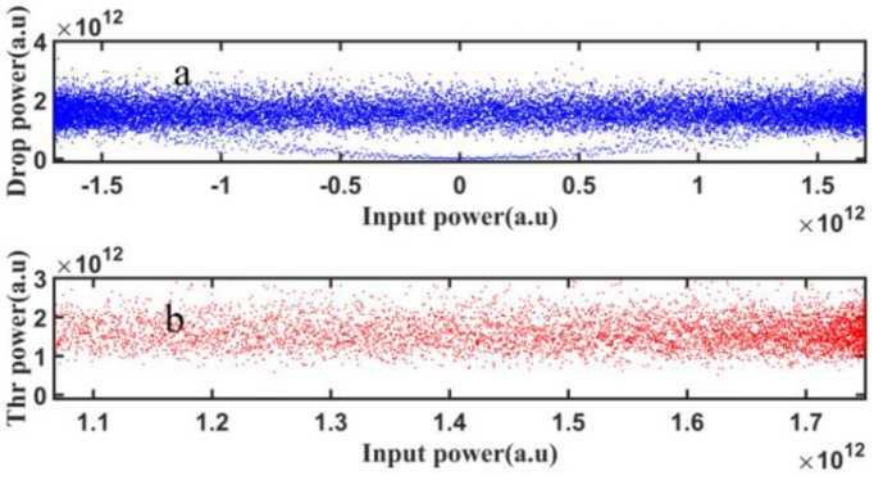

Figure 22: A Panda-ring's response for plane wave input light and bright soliton at add port, where (a) drop against input and (b) through against input.

We have proposed a concept of using a soliton modulated circuit regarding a few advantages, which are (i) the soliton source wavelength, (ii) the applied antenna is within the radio wave does not interfere with the currently applied frequency bands from other transmissions, and (iii) various potential applications. Further, the new material called a chalcogenide glass can be used to form the circuit, from which the wavelength range can be extended to cover the radio wave frequency. From the obtained simulation results of a modified add-drop multiplexing circuit, which is a tiny device that can be fabricated and integrated to be a signal transmission node. In this case, the connection between vehicles in the road traffic can be applied by the micro antenna, which is not our proposed work. We are concentrated on the link from one node to others along the road (side road) by using the free-space link, of course, a soliton transmission is recommended. The transmission from vehicles-to-vehicles nodes to vehicles can be employed by the same antenna. By using the proposed concept, the communication coverage area can be of 1 km radius, which means that the free-space transmission to the train and helicopter can also be applied. Moreover, the link of nodes to the underground train is also available. Soliton communication is, of course, the available power can be used with the high capacity and reliability. In some cases, if cable transmission is required, it is also suitable. More applications to the designed circuit such as multiplexing, modulating, filtering can also be done via the specified input ports. The transmission based-on security using the chaotic and bifurcation signals are also available, while the quantum cryptography can also be applied due to the soliton property that the

entangle soliton can be generated and applied by the bright and dark soliton conversion aspect.

4. Conclusion

This paper proposed the very challenging system of a soliton modulated source within a microring add-drop multiplexer. The device materials are GaAsInP-InP and SOI that are commercially available, in which the device scales are within the fabrication ability. A soliton power itself can be used for a long-distance transmission node. From the obtained results have shown that there are various forms of the inputs and outputs suitable for the proposed applications. We have recommended using for a LiFi V2X connection nodes, which is suitable for the side road of the traffic. Moreover, the applications for the sky and underground link within the link radius of 1 km is also plausible.

References

[1] Haas, H. (2018). LiFi is a paradigm-shifting 5G technology. Reviews in Physics, 3, 26-31.

[2] Boccardi, F., Heath, R. W., Lozano, A., Marzetta, T. L. and Popovski, P. (2014). Five disruptive technology directions for 5G. IEEE communications magazine, 52(2), 74-80.

[3] Tsonev, D., Videv, S. and Haas, H. (2015). Towards a 100 Gb/s visible light wireless access network. Optics express, 23(2), 1627-1637.

[4] Ni, W., Liu, R. P., Collings, I. B. and Wang, X. (2013). Indoor cooperative small cells over ethernet. IEEE Communications Magazine, 51(9), 100-107.

[5] Wang, Z., Tsonev, D., Videv, S. and Haas, H. (2015). On the design of a solar-panel receiver for optical wireless communications with simultaneous energy harvesting. IEEE Journal on Selected Areas in Communications, 33(8), 1612-1623.

[6] Mitola, J. and Maguire, G. Q. (1999). Cognitive radio: making software radios more personal. IEEE personal communications, 6(4), 13-18.

[7] Khalid, A. M., Cossu, G., Corsini, R., Choudhury, P. and Ciaramella, E. (2012). 1-Gb/s transmission over a phosphorescent white LED by using rate-adaptive discrete multitone modulation. IEEE photonics journal, 4(5), 1465-1473.

[8] Haas, H., Yin, L., Wang, Y. and Chen, C. (2015). What is lifi?. Journal of lightwave technology, 34(6), 1533-1544.

[9] Wu, L., Zhang, Z., Dang, J. and Liu, H. (2014). Adaptive modulation schemes for visible light communications. Journal of Lightwave Technology, 33(1), 117-125.

[10] Nguyen, T., Islim, M. S., Cheng, C., & Haas, H. (2021, September). Spectral Efficient and High Performance LiFi Color Dimming. In 2021 IEEE 94th Vehicular Technology Conference (VTC2021-Fall) (pp. 1-6). IEEE.

[11] Kim, J. K. and Schubert, E. F. (2008). Transcending the replacement paradigm of solid-state lighting. Optics Express, 16(26), 21835-21842.

[12] Park, J. (2010). Speedup of dynamic response of organic light-emitting diodes. Journal of Lightwave Technology, 28(19), 2873-2880.

[13] Quintana, C., Guerra, V., Rufo, J., Rabadan, J. and Perez-Jimenez, R. (2013). Reading lamp-based visible light communication system for in-flight entertainment. IEEE Transactions on Consumer Electronics, 59(1), 31-37.

[14] Rajagopal, S., Roberts, R. D. and Lim, S. K. (2012). IEEE 802.15. 7 visible light communication: modulation schemes and dimming support. IEEE Communications Magazine, 50(3), 72-82.

[15] Rajbhandari, S., Chun, H., Faulkner, G., Cameron, K., Jalajakumari, A. V., Henderson, R., ... and O'Brien, D. (2015). High-speed integrated visible light communication system: Device constraints and design considerations. IEEE Journal on Selected Areas in Communications, 33(9), 1750-1757.

[16] Huang, W., Gong, C. and Xu, Z. (2015). System and waveform design for wavelet packet division multiplexing-based visible light communications. Journal of Lightwave Technology, 33(14), 3041-3051.

[17] Farid, A. A. and Hranilovic, S. (2010). Capacity bounds for wireless optical intensity channels with Gaussian noise. IEEE Transactions on Information Theory, 56(12), 6066-6077.

[18] Gomez, A., Shi, K., Quintana, C., Sato, M., Faulkner, G., Thomsen, B. C. and O'Brien, D. (2014). Beyond 100-Gb/s indoor wide field-of-view optical wireless communications. IEEE Photonics Technology Letters, 27(4), 367-370.

[19] MacHardy, Z., Khan, A., Obana, K. and Iwashina, S. (2018). V2X access technologies: Regulation, research, and remaining challenges. IEEE Communications Surveys & Tutorials, 20(3), 1858-1877.

[20] Katsaros, K., Dianati, M., Tafazolli, R. and Guo, X. (2015). End-to-end delay bound analysis for location-based routing in hybrid vehicular networks. IEEE Transactions on Vehicular Technology, 65(9), 7462-7475.

[21] Araniti, G., Campolo, C., Condoluci, M., Iera, A. and Molinaro, A. (2013). LTE for vehicular networking: a survey. IEEE communications magazine, 51(5), 148-157.

[22] Sichitiu, M. L. and Kihl, M. (2008). Inter-vehicle communication systems: a survey. IEEE Communications Surveys & Tutorials, 10(2), 88-105.

[23] Alsabaan, M., Alasmary, W., Albasir, A. and Naik, K. (2012). Vehicular networks for a greener environment: A survey. IEEE Communications Surveys & Tutorials, 15(3), 1372-1388.

[24] Zheng, K., Zheng, Q., Chatzimisios, P., Xiang, W. and Zhou, Y. (2015). Heterogeneous vehicular networking: A survey on architecture, challenges, and solutions. IEEE communications surveys & tutorials, 17(4), 2377-2396.

[25] Petit, J., Schaub, F., Feiri, M. and Kargl, F. (2014). Pseudonym schemes in vehicular networks: A survey. IEEE communications surveys & tutorials, 17(1), 228-255.

[26] Qu, F., Wu, Z., Wang, F. Y. and Cho, W. (2015). A security and privacy review of VANETs. IEEE Transactions on Intelligent Transportation Systems, 16(6), 2985-2996.

[27] Hadded, M., Muhlethaler, P., Laouiti, A., Zagrouba, R. and Saidane, L. A. (2015). TDMA-based MAC protocols for vehicular ad hoc networks: a survey, qualitative analysis, and open research issues. IEEE Communications Surveys & Tutorials, 17(4), 2461-2492.

[28] Chen, S., Hu, J., Shi, Y. and Zhao, L. (2016). LTE-V: A TD-LTE-based V2X solution for future vehicular network. IEEE Internet of Things journal, 3(6), 997-1005.

[29] Fettweis, G. P. (2014). The tactile internet: Applications and challenges. IEEE vehicular technology magazine, 9(1), 64-70.

[30] Vicente-Lozano, M., Franceschetti, G., Ares-Pena, F. J. and Moreno-Piquero, E. (2002). Analysis and synthesis of a printed array for satellite communication with moving vehicles. IEEE transactions on antennas and propagation, 50(11), 1555-1559.

[31] Hafeez, K. A., Anpalagan, A. and Zhao, L. (2015). Optimizing the control channel interval of the dsrc for vehicular safety applications. IEEE Transactions on Vehicular Technology, 65(5), 3377-3388.

[32] Raya, M., Papadimitratos, P., Aad, I., Jungels, D. and Hubaux, J. P. (2007). Eviction of misbehaving and faulty nodes in vehicular networks. IEEE Journal on Selected Areas in Communications, 25(8), 1557-1568.

[33] Seo, H., Lee, K. D., Yasukawa, S., Peng, Y. and Sartori, P. (2016). LTE evolution for vehicle-to-everything services. IEEE communications magazine, 54(6), 22-28.

[34] Heebner, J. E., Boyd, R. W. and Park, Q. H. (2002). SCISSOR solitons and other novel propagation effects in microresonator-modified waveguides. JOSA B, 19(4), 722-731.

[35] Bahadoran, M., Ali, J. and Yupapin, P. P. (2013). Graphical approach for nonlinear optical switching by PANDA vernier filter. IEEE Photonics Technology Letters, 25(15), 1470-1473.

[36] Bahadoran, M., Aziz, M., Noorden, A., Jalil, M., Ali, J. and Yupapin, P. (2014). Novel approach to determine the Young's modulus in silicon-on-insulator waveguide using microring resonator. Digest Journal of Nanomaterials and Biostructures, 9(3), 1095-1104.

[37] Mikroulis, S., Simos, H., Roditi, E. and Syvridis, D. (2005). Ultrafast all-optical AND logic operation based on four-wave mixing in a passive InGaAsP-InP microring resonator. IEEE photonics technology letters, 17(9), 1878-1880.

[38] Koos, C., Jacome, L., Poulton, C., Leuthold, J. and Freude, W. (2007). Nonlinear silicon-on-insulator waveguides for all-optical signal processing. Optics Express, 15(10), 5976-5990.